Polymer 112 (2017) 76–86

Contents lists available at ScienceDirect

Polymer

journal homepage: www.elsevier.com/locate/polymer

Probing the confining effect of clay particles on an amorphous intercalated dendritic polyester

Kevin P. Meyers [a], Jeremy J. Decker [a], Brian G. Olson [a], Jun Lin [b], Alexander M. Jamieson [c], Sergei Nazarenko [a, *]

[a] School of Polymers and High Performance Materials, University of Southern Mississippi, Hattiesburg, MS 39406, United States
[b] Renewable Energy School, North China Electric Power University, Beijing, China
[c] Department of Macromolecular Science and Engineering, Case Western Reserve University, Cleveland, OH 44106, United States

ARTICLE INFO

Article history:
Received 21 October 2016
Received in revised form
18 January 2017
Accepted 26 January 2017
Available online 27 January 2017

Keywords:
Nanocomposite
Positron annihilation lifetime spectroscopy
Intercalation
Hyperbranched polymer
Rigid amorphous fraction

ABSTRACT

The fourth generation of a hydroxylated dendritic hyperbranched polyester (HBP) was combined with sodium montmorillonite clay (Na^+MMT) using water to generate a broad range of polymer clay nanocomposites from 0 to 100% wt/wt Na^+MMT. Analysis with differential scanning calorimetry (DSC) showed a deviation in heat capacity, ΔC_p, with clay content at the T_g from a two-phase trend which was attributed to the formation of an immobilized rigid amorphous fraction (RAF) in the interlayer spacing of the intercalated system. This deviation occurred in a step-like fashion which we attributed to 0.5 nm incremental changes in the interlayer spacing, previously observed through X-ray diffraction analysis. A simple series model was utilized to quantify these interlayer spacings based on the ΔC_p values and showed good correspondence with the X-ray results. The RAF was quantified from changes in heat capacity with clay content and was verified by an alternative novel positron annihilation lifetime spectroscopy (PALS) approach. The PALS quantification of the RAF was possible through an analysis of changes in the hole size thermal expansivity of the nanocomposites as a function of clay composition. Results indicated that as much as 32% by weight of the system is made up of the RAF at its maximum.

1. Introduction

Polymer clay nanocomposites often exhibit chemical and physical properties that are superior to those of conventional composite materials [1–3]. The morphology of these nanocomposites can generally be classified as phase separated, intercalated, disordered intercalated, or exfoliated, depending on the interactions between the nanoclay and the polymer as well as the processing conditions [1–3]. To promote dispersion in a polymer matrix, layered silicates such as sodium montmorillonite (Na^+MMT) typically require modification by surfactants to increase the organophilicity of the clay surfaces.

Various water-soluble linear polymers, such as poly(ethylene oxide) (PEO), poly(vinyl alcohol) (PVA), and poly(vinylpyrrolidinone) (PVP), have successfully been intercalated into unmodified Na^+MMT clay galleries by aqueous solution casting methodologies [1,2]. However, the high viscosities of these systems can require shear intensive processing procedures, especially at high clay contents [4]. Hyperbranched polymers (HBPs) possess lower solution viscosities than linear polymers due to their more compact globular structures [5], which facilitate solution processing, even at high clay concentrations, without shear intensive procedures.

Due to their facile synthesis [6–9], dendritic hyperbranched polyester polyols (also known as Boltorn™ dendritic polyols) based on 2,2-bis-methylopropionic acid (bis-MPA) with an ethoxylated pentaerythritol core are popular model systems which preserve the essential features of dendrimers, namely high end-group functionality and a globular architecture, but possess imperfect branching and large polydispersities [5–16]. These HBPs are hydrophilic due to the presence of branch-terminal hydroxylated end groups [17], and hence are compatible with clay gallery surfaces. Experimental [18–22] and theoretical [23] studies indicate that a high interaction strength between the end functional groups of the dendritic polymers and a substrate leads to the collapse and flattening of the globular dendritic structure on the substrate.

The incorporation of polymer into clay galleries exposes numerous interfaces to the polymer matrix and the resulting polymer-substrate interactions can be probed by bulk techniques. Månson et al. [24–27] explored the structure of intercalated

* Corresponding author.
E-mail address: Sergei.Nazarenko@usm.edu (S. Nazarenko).

http://dx.doi.org/10.1016/j.polymer.2017.01.065
0032-3861/

nanocomposite films based on surfactant-free Na^+MMT clays mixed with second, third, and fourth pseudogeneration Boltorn™ dendritic polyols. X-ray diffraction (XRD) data demonstrated that, at intermediate Na^+MMT contents, the interlayer spacings of the intercalated nanocomposites correlated closely with estimates of the molecular diameters of the different HBP generations. It was concluded that the HBPs maintained their globular architecture in an intercalated state throughout approximately half of the compositional range. However, at the higher clay contents, the HBPs flattened within the clay galleries, leading to equivalent interlayer spacings for the 2nd, 3rd, and 4th HPB generations.

Subsequently, we carried out a more detailed morphological analysis of the same intercalated nanocomposite system [28], specifically comprising of the 2nd and 4th pseudogenerations of Boltorn dendritic polyols and ecompassing polymer clay nanocomposite compositions from 0 to 95% wt/wt Na^+MMT. Intercalation peaks were observed by powder XRD at and above 15% wt/wt Na^+MMT content for both HBP systems. In fact, intercalation was present at all clay loadings, as evidenced by TEM, but, at lower clay contents, exfoliated and disordered intercalated states were also present. The number of clay layers per intercalated stack increased with increases in Na^+MMT content. The interlayer spacings for the 2nd and 4th pseudogenerations (HBP2 and HBP4) were observed to decrease in increments of approximately 0.5 nm as the clay content increased. Importantly, the interlayer spacings for the 2nd and 4th generations of HBP were nearly identical at the same clay compositions, indicative that the interlayer spacings were independent of the HBP generation number. The interlayer spacings for both HBP2 and HBP4 decreased with increasing clay content until finally reaching a minimum spacing of 0.5 nm at the highest clay contents. These step-wise changes in interlayer spacings are consistent with the presence of discrete layers of flattened HBP between the clay layers. It was proposed that the HBP adsorbed onto the clay layers in solution and re-aggregated, upon solvent removal, into intercalated stacks of clay and flattened HBP. Recently, layer-by-layer intercalation of flattened Boltorn™ HBPs into Na^+MMT clay galleries was confirmed by Androulaki et al. [29]. Analogous behavior was observed for Na^+MMT clay based nanocomposites with a hyperbranched polyesteramide (Hybrane™) and a polyamidoamine (PAMAM) dendrimer, each prepared via aqueous solution intercalation methodology [30,31]. Therefore, this trend appears to be fairly general for hydrophilic dendritic systems.

The confinement of collapsed HBP between multiple clay layers is expected to result in a sizable amount of immobilized polymer. The nature of this immobilized polymer is viewed as analogous to the concept of a rigid amorphous fraction (RAF) in semi-crystalline polymers, introduced to explain an observed discrepancy between the degree of crystallinity and the change in heat capacity, ΔC_p, at the glass transition, T_g [32]. In simplest terms, RAF represents the fraction of the amorphous phase that does not contribute to the change in ΔC_p at either the T_g or T_m (melting). It is well-established [32–44] that the RAF is due to an immobilization of the disordered polymer chains that connect the crystalline lamellae. These chains are unable to undergo long range translational motions when crystalline constraints are imposed during crystallization of the polymer melt, implying that the RAF vitrifies in the vicinity of the crystallization temperature, T_c. In contrast, the un-constrained amorphous chains, the mobile amorphous fraction (MAF), remain in the molten state at T_c and vitrify upon cooling at the regular T_g. Complete devitrification of RAF occurs at T_m.

It is also established that the immobilized amorphous phase in nanocomposites exhibits some of the characteristics of a RAF, such as the suppression of the glass transition [45–48]. The majority of recent research on RAF at the particle interface has involved SiO_2 nanocomposites that utilize ΔC_p analysis at the T_g to measure the amount of RAF [49–54] and has focused on semicrystalline polymer nanocomposite systems [55–61].

Unlike crystalline phases, however, inorganic clay does not melt within the thermal stability range of the polymers. This means that, if the interactions between polymer and inorganic substrate are maintained at elevated temperatures, devitrification of the immobilized chains does not occur [45]. Indeed, this was demonstrated in a study of the dynamics of an amorphous hyperbranched polyesteramide intercalated in Na^+MMT layers via quasi elastic-neutron scattering [62]. It was observed that the polymer chains confined within the clay galleries exhibit dynamical behavior above the bulk T_g similar to that of the bulk polymer below the T_g. The HBP dynamics were frozen due to the clay nanoconfinement, consistent with observed decreases in ΔC_p at the T_g [62].

In the current paper we study the behavior of the immobilized RAF in surfactant-free Na^+MMT clay nanocomposites generated using the 4th generation of a Boltorn™ dendritic polyol over a very broad range of compositions (0–100% wt/wt). Since the Na^+MMT exhibits no thermal transitions within the investigated temperature ranges, it is ideally suited to investigate polymer immobilization solely at the clay interfaces. Heat capacity measurements were used to quantify the amount of RAF as described by Wunderlich et al. for semicrystalline polymers [32]. We demonstrate that the heat capacity behavior shows a strong correlation with the earlier observed step-like behavior of interlayer spacing in these intercalated nanocomposites [28,29]. To probe the structure of the RAF, free volume measurements using positron annihilation life-time spectroscopy (PALS) were employed.

PALS is a well-established, quantitative probe for free volume in polymeric materials [63,64]. In a PALS experiment, high energy positrons are injected from a radiation source into a polymer sample. The positrons thermalize via collisions with atoms and either annihilate or form a hydrogen-like pair with a secondary electron created via collision-induced ionization. In polymers, the more stable pair system, called an ortho-positronium (o-Ps), tends to localize in regions of low density, i.e. holes. Annihilation of such localized o-Ps occurs via a pickoff mechanism in which the o-Ps positron annihilates with an electron of the medium with an opposite spin. Quantitative comparisons have been established between the characteristic parameters, obtained via PALS, viz. the intensity, I_3, and lifetime, τ_3, of the o-Ps annihilation component, and the fractional free volume, f_v, of amorphous polymers, as computed by statistical mechanical theory [65,66]. The o-Ps intensity, I_3, is typically regarded as a measure of the number density of the free volume holes. The o-Ps lifetime, τ_3, can be related to a spherical hole radius, R, via the Tao-Eldrup equation, which is based on quantum mechanical and empirical arguments [67,68] as follows:

$$\tau_3 = 0.5\,(ns)\left[1 - \frac{R}{R_0} + \frac{1}{2\pi} sin\left(\frac{2\pi R}{R_0}\right)\right]^{-1} \quad (1)$$

where R is the hole radius in Ǻ. R_0 equals $R + \Delta R$ where ΔR is a fitted empirical electron layer thickness of 1.66 Å. From R, the average hole free volume $v_h = (4\pi/3)R^3$ may be calculated. It follows that f_v is proportional to the product $I_3 v_h$.

As mineral silicate layers are too dense for o-Ps species to form, PALS is only sensitive to the HBP content of the HBP/clay nanocomposites. PALS experiments were used to assess, as a function of clay content, the average free volume hole size below and above the glass transition of the nanocomposites. The broad range of compositions prepared in this study enabled a novel opportunity to examine the free-volume behavior in intercalated polymer/clay nanocomposites. We anticipated that the RAF, which remains in the vitrified state above T_g, and the MAF, which becomes liquid at $T > T_g$, contribute in an additive fashion to the overall hole volume thermal expansion coefficient. Therefore, we looked forward to estimate the amount of RAF in the nanocomposites by PALS, and hence verify the DSC methodology based on the measurements of ΔC_p at the T_g.

2. Experimental

2.1. Materials and sample preparation

Sodium montmorillonite clay (Na^+MMT) Cloisite® with a cation exchange capacity (CEC) of 92.6 meq/100 g was purchased from Southern Clay Products. As received clay powder was sifted through a 75 micron sieve, dried at 150 °C under vacuum overnight, and stored over desiccant prior to use. The hydroxyl-functional dendritic hyperbranched polyester, Boltorn™ H40 (HBP4), was obtained from Perstorp Specialty Chemicals AB in the form of pellets. A schematic representation of the hyperbranched structure of HBP4 is shown in Schematic 1.

The nanocomposites utilized in this study were created via a solution-intercalation method and were from the same batches investigated previously [28]. The required amount of Na^+MMT clay was first dispersed in deionized water at 50 °C and stirred for at least 8 h to optimize clay delamination. The aqueous concentration of the clay was kept below 1% wt/wt in order to ensure that individual clay layers were well dispersed. When sufficiently diluted, Na^+MMT particles are known to delaminate into single layers [69].

The required amount of Boltorn™ polyol was dissolved in boiling DI water. The concentration of polymer in water was kept at or below 10% wt/wt as this concentration was observed to effectively disperse and dissolve the HBP4. This solution was then quantitatively transferred into the clay dispersion. This combined solution was rapidly stirred in open air at 50 °C until the dispersion approached the level of the stir bar but remained in a liquid state. It was then transferred to Teflon trays and dried for two days in a convection oven at 50 °C. Two further days of drying followed, under vacuum, at 120 °C. This temperature was demonstrated as optimal for removing water from Boltorn™ polyols [70]. The resulting nanocomposite films were stored over desiccant at room temperature. The mineral volume fraction of clay in the nanocomposites, ϕ_m, was calculated from the corresponding mineral weight fractions, w_m, and the nanocomposite densities were measured by a buoyancy method as reported in our previous publication [28]. As also reported in our previous study, no changes in density of the amorphous HBP4 were observed in the nanocomposites [28].

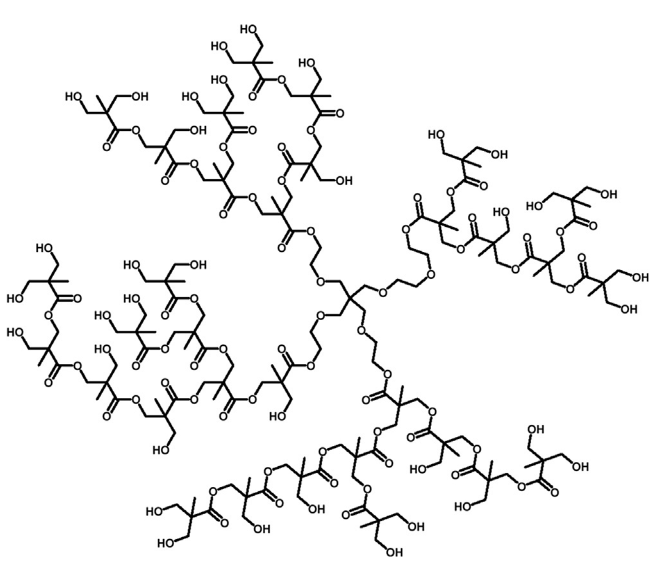

Schematic 1. Example of a fourth generation hydroxyl-functional dendritic hyperbranched polyester, Boltorn™ H40 (HBP4) accounting for imperfect branching.

2.2. Characterization

The thermal behavior of the nanocomposite and control films was evaluated using a TA Instruments Q2000 Differential Scanning Calorimeter. Heating and cooling scans were carried out at a 10 °C/min rate over a range of −50 to 150 °C under a dry nitrogen atmosphere. The nanocomposites were taken directly from the desiccator and placed into sealed aluminum pans to prevent water uptake. Second heating scans were utilized for the analysis to eliminate any physical ageing effects. Second and third heating scans were self-consistent. The T_g of the nanocomposites and the ΔC_p, at T_g, were determined according to previously established methodology reported elsewhere [71,72]. The T_g was taken as the point where half of the polymer was devitrified as determined from the heat capacity increase, where a line drawn median to the heat capacity lines for the glass and liquid behavior intersects the DSC curve.

The positron annihilation lifetime spectroscopy (PALS) experiments were conducted using a fast-fast coincidence system with a time resolution of 220 ps. 1×1 cm^2 area pieces were cut from each sample film for analysis. On each side of a 30 μCi ^{22}Na positron source, pieces of the sample films were stacked to a total thickness of 1 mm. The sample cell was kept under vacuum during the experiments. All measurements were taken over one hour, for a total of 1×10^6 counts in each PALS spectrum. Temperature measurements were taken by first decreasing the temperature to −30 °C then waiting for one hour to allow for equilibrium before beginning the first experiment. The temperature was then sequentially increased in 10 °C steps, collecting a spectrum at each step, after waiting 10 min to allow for equilibration. The PALS spectra were tested against three and four component fits using the PATFIT 88 software package [73].

For transmission electron microscopy (TEM), the nanocomposite films were embedded in epoxy resin and microtomed. Approximately 90 nm thick sections were cut at −30 °C perpendicular to the film surface using a Leica cryo-ultramicrotome FC6 equipped with freshly cut glass knives. These sections were imaged using a Zeiss 109T TEM operated at 80 kV under bright field conditions. Since the silicate layers possess a higher electron density than the surrounding HBP matrix, they appear darker in the images.

3. Results and Discussion

3.1. Probing the amorphous phase of nanocomposites by DSC

Representative thermal scans of the nanocomposite systems and the pure HBP4 control are shown in Fig. 1. The HBP4 control exhibited a glass transition temperature at 24.2 ± 1.2 °C followed first by exothermic and then endothermic events with corresponding minima and maxima at around 70 °C and 110 °C. Žagar et al. previously attributed these exo- and endo-events to the formation and cleavage of H-bonds between multiple hydroxyl groups [9,10]. However, our most recent results, to be reported in a forthcoming publication, led us to attribute the exothermic and endothermic events, respectively, to the formation and melting of an ordered mesophase involving the lateral attachment of the HBP linear segments, via hydroxyl-hydroxyl or hydroxyl-carbonyl group H-bonding. The magnitude of these exo and endo events dramatically decreased with clay content until they were completely

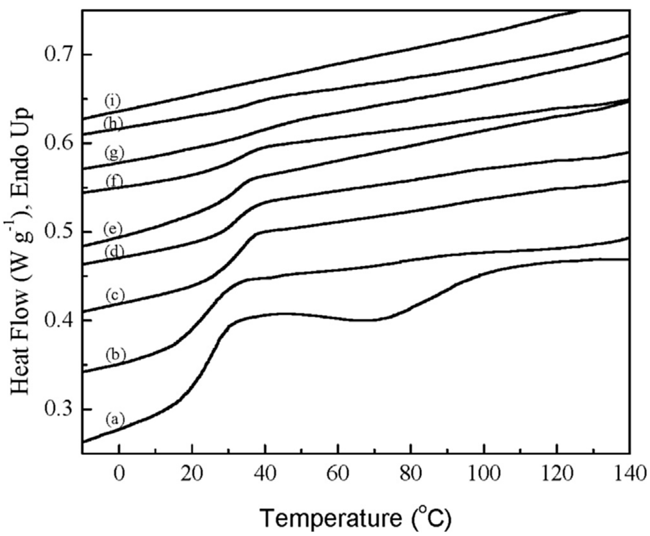

Fig. 1. DSC thermograms of HBP4/Na$^+$MMT nanocomposites with different clay loading a) 0 wt%, b) 10 wt%, c) 20 wt%, d) 30 wt%, e) 40 wt%, f) 50 wt%, g) 60 wt%, h) 70 wt%, and i) 80 wt% Na$^+$MMT. Curves vertically offset to aid the viewer.

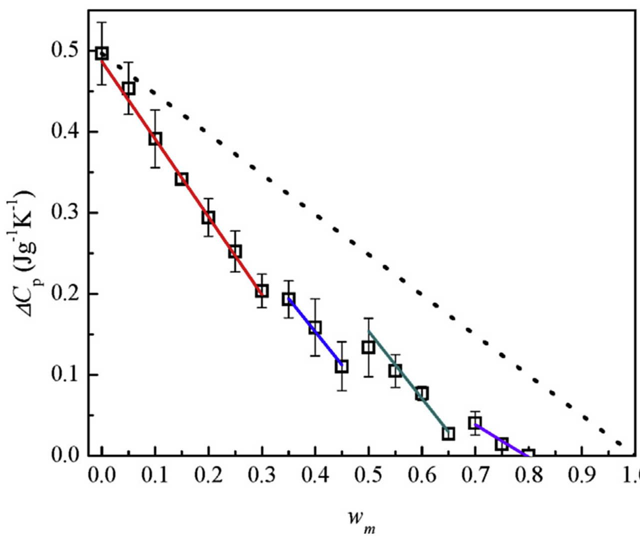

Fig. 2. ΔC_p at T_g for HBP4 nanocomposites as a function of Na$^+$MMT weight fraction, w_m. The dashed line represents the standard two-phase model prediction. Error bars represent standard deviations from multiple DSC runs. The colored shifted striations help visualize the step-wise changes in ΔC_p.

undetectable above 20% wt/wt Na$^+$MMT, suggesting that adding clay suppresses the formation of the mesophase, likely due to a disruption of the interchain H-bonding under confinement. Consistent with this interpretation, based on the measurements of the activation energy for the dielectric γ-relaxation, which is due to the hydroxyl group motions in similar nanocomposites, Androulaki et al. concluded [29] that the flattening of dendritic HBPs in the presence of clay surfaces impedes H-bond formation.

The bulk T_g exhibited a moderate, approximately 12 °C, increase while the ΔC_p at T_g decreased dramatically with the addition of clay (Fig. 1). At 80% wt/wt and higher clay content, the glass transition in the nanocomposites was fully suppressed. The measured T_g and ΔC_p at T_g are displayed in Table 1. Standard deviations listed are based on numerous discrete DSC measurements made on each sample. Fig. 2 depicts the heat capacity changes for the nanocomposites as a function of weight fraction of Na$^+$MMT, w_m. In the case of a two phase composite system consisting of an amorphous polymer phase and inorganic clay particles, the ΔC_p can be expected to decrease linearly with the clay content as depicted by the dashed line in Fig. 2. However, in reality, the ΔC_p behavior for the nanocomposites deviated significantly from this linear trend. The segmental mobility of a considerable portion of the amorphous HBP polymer is clearly suppressed in the presence of the clay surfaces.

The deviation from the two-phase prediction in Fig. 2 grew in significance as the clay content increased linearly to approximately 30% wt/wt, then exhibited a series of step-like decreases, punctuated by linear increases, which can be seen in Fig. 2 as the colored shifted linear striations. These linear groupings will be described in more depth later, but are attributed to the different intercalation interlayer spacing groups as shown in Fig. 3 and depicted as color-coordinated layers in Schematic 2. For each group, the ΔC_p deviates increasingly from the two phase model as more clay layers per tactoid allow for more constrained polymer. This trend follows with increasing clay content until the interlayer spacing changes (decreases) and an increase in the amount of unconstrained polymer is observed as there is less polymer immobilized between each clay

Table 1
Glass transition temperatures (T_g), changes in heat capacity (ΔC_p), and calculated amorphous fractions with Na$^+$MMT content.

Weight fraction Na$^+$MMT (w_m)	Volume fraction Na$^+$MMT (φ_m)	Glass transition temperature ± std deviation (T_g)	Heat capacity jump at T_g ± std deviation (ΔC_p)	Rigid amorphous fraction (w_{RAF})	Mobile amorphous fraction (w_{MAF})
0.00	0.000	24.2 ± 1.2	0.497 ± 0.038	0.0	1.0
0.05	0.023	23.6 ± 1.2	0.453 ± 0.032	0.04 ± 0.09	0.91 ± 0.09
0.10	0.048	24.7 ± 0.5	0.391 ± 0.036	0.11 ± 0.09	0.79 ± 0.09
0.15	0.075	29.2 ± 1.2	0.342 ± 0.006	0.16 ± 0.05	0.69 ± 0.05
0.20	0.102	31.4 ± 1.0	0.294 ± 0.023	0.21 ± 0.06	0.59 ± 0.06
0.25	0.132	30.4 ± 0.7	0.252 ± 0.025	0.24 ± 0.06	0.51 ± 0.06
0.30	0.164	31.7 ± 1.2	0.203 ± 0.011	0.29 ± 0.04	0.41 ± 0.04
0.35	0.197	31.7 ± 0.7	0.193 ± 0.023	0.26 ± 0.05	0.39 ± 0.05
0.40	0.233	30.7 ± 0.6	0.158 ± 0.035	0.28 ± 0.07	0.32 ± 0.07
0.45	0.272	32.3 ± 1.6	0.110 ± 0.030	0.33 ± 0.06	0.22 ± 0.06
0.50	0.313	29.2 ± 1.4	0.134 ± 0.036	0.23 ± 0.08	0.27 ± 0.08
0.55	0.358	30.4 ± 1.1	0.105 ± 0.020	0.24 ± 0.04	0.21 ± 0.04
0.60	0.406	37.8 ± 2.8	0.077 ± 0.008	0.25 ± 0.02	0.15 ± 0.02
0.65	0.459	35.0 ± 1.4	0.027 ± 0.007	0.30 ± 0.01	0.05 ± 0.01
0.70	0.516	36.0 ± 0.8	0.040 ± 0.015	0.22 ± 0.03	0.08 ± 0.03
0.75	0.578	36.3 ± 2.3	0.014 ± 0.006	0.22 ± 0.01	0.03 ± 0.01
0.80	0.646	NA	0.000 ± 0.000	0.20	0

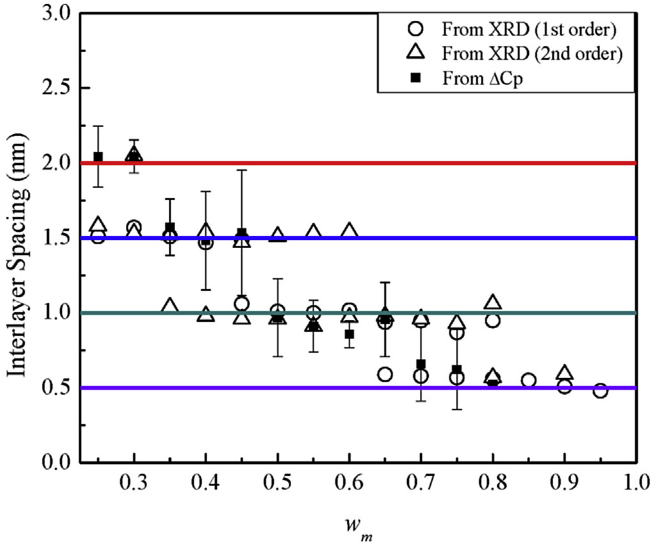

Fig. 3. Interlayer spacings predicted using Eqn. (3) (■), calculated from the experimentally determined values for ΔC_p at T_g. Interlayer spacings observed directly by XRD for the powdered HBP4 nanocomposites (1st order diffraction, ○, and 2nd order diffraction, Δ) are also plotted as a function of weight fraction Na^+MMT. Error bars represent the error propagated from the ΔC_p determinations. Colored gridlines represent the differentiated nanocomposite groupings with different interlayer spacings as observed in Fig. 2.

layer.

The weight fraction of the amorphous polymer phase which contributed to the step in the heat capacity at T_g, mobile amorphous fraction (MAF), was calculated based on the corresponding ΔC_p for the nanocomposite and ΔC_p^o for the pristine HBP4 polymer, $w_{MAF} = \frac{\Delta C_p}{\Delta C_p^o}$. The fraction of the immobilized amorphous phase, the rigid amorphous fraction (RAF), of the HPB4 polymer was calculated assuming $w_m + w_{RAF} + w_{MAF} = 1$ [32, 74–75].

As mentioned previously, we attributed the step-like ΔC_p behavior (the colored striations in Fig. 2) to the step-like intercalation behavior. Naturally, a question was posed if the step-like interlayer spacing variations can be directly calculated from the ΔC_p behavior. The highly ordered intercalated morphology of the nanocomposites enabled us to consider a simple series model in which multiple confined polymer layers are alternated between mineral layers.

We assume that the interlayers are composed entirely of RAF with the thickness of these layers designated as h_{RAF}. The volume of the clay can be expressed as, $V_m = nL_mW_mh_m$, where n equals the number of MMT layers and W and L represent the length and width of the clay stacks respectively. The thickness of the individual MMT layers, h_m, was previously determined to be 0.96 nm. The large lateral dimensions of the clay far exceed the 1 nm layer thickness; therefore edge effects were neglected in this analysis. Since the RAF is assumed to be only within the MMT stacks, the volume of RAF can be expressed as $V_{RAF} = (n-1)L_{RAF}W_{RAF}h_{RAF}$. Complete surface coverage of the MMT layers by the RAF is assumed within these stacks, thus L and W for the RAF and MMT are assumed equal and the ratio of V_{RAF}/V_m, which directly relates the heights of the RAF and MMT layers, can be expressed as:

$$\frac{V_{RAF}}{V_m} = \frac{(n-1)h_{RAF}}{nh_m} \approx \frac{h_{RAF}}{h_m} \tag{2}$$

TEM observations confirm that the number of layers in the intercalated stacks increases with clay content to an extent that enable us to simplify Eqn. (2) by removing the necessity to know the precise number of clay layers. Supplementary Fig. 1 shows through high and low resolution TEM micrographs that above 15% wt/wt the number of clay layers per stack is greater than 10 (~15–20). This simplification will likely not hold at low clay loadings. By combining Eqn. (2) with the heat capacity prediction stated previously, $w_{MAF} = \frac{\Delta C_p}{\Delta C_p^0}$, and solving for h_{RAF}, an equation was established where the interlayer spacing can be calculated from the observed ΔC_p values, determined by DSC, and the known clay compositions.

$$h_{RAF} = \frac{\left(1 - w_m - \Delta C_p / \Delta C_p^0\right) h_m \rho_m}{\rho_{RAF} w_m} \tag{3}$$

As detailed in our previous publication, no changes in density of the HBP4 were observed in the nanocomposites [28]. Therefore, the densities of the MAF, ρ_{MAF}, and the RAF, ρ_{RAF}, were assumed to be identical with a value of 1.306 g/cm^3. A density, ρ_m, of 2.86 g/cm^3 was employed for the Na^+MMT Cloisite® mineral layers in these calculations.

Fig. 3 shows the consistency between the interlayer spacings observed by XRD and those calculated from Eqn. (3). Moreover, the step-wise nature of the interlayer spacing correlates to the steps observed in Fig. 2 as marked by the linearly off-set striations for

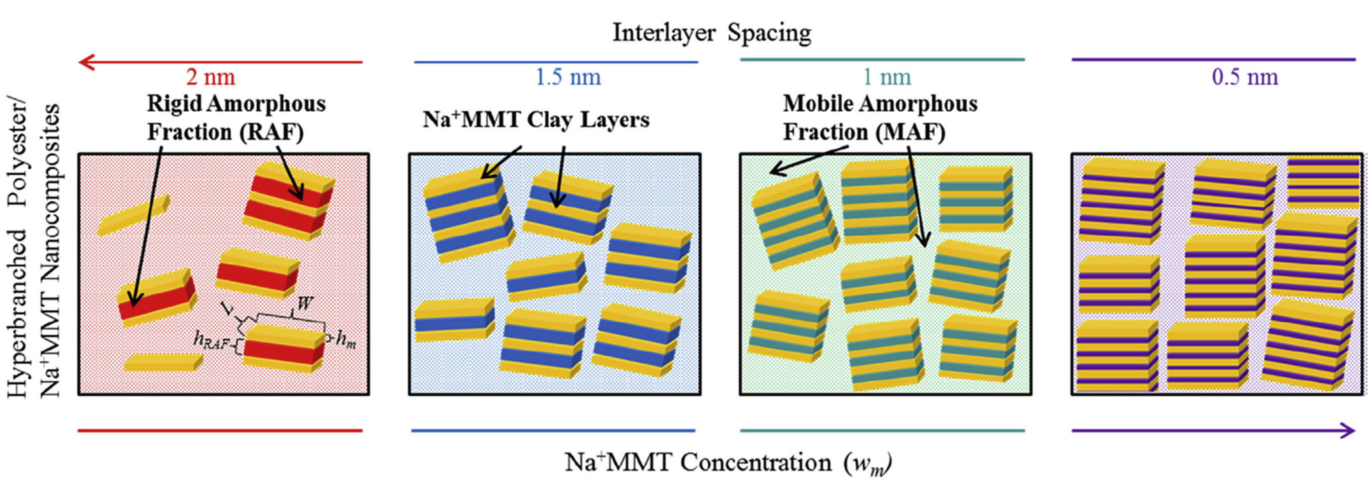

Schematic 2. Depiction of the decrease in the intercalated clay interlayer spacing with increased clay concentration. The different colors of the confined polymer phase (RAF) represent groupings of nanocomposite concentrations with distinct interlayer spacing thicknesses from 2 to 0.5 nm. The MAF is represented by the patterned lighter shaded area surrounding the clay tactoids.

clarity. Note, the proposed DSC based analysis does not mirror the fact that different intercalated states can coexist in a given nanocomposite leading to two distinct intercalation peaks on the same diffractogram [28]. One plausible argument, why despite this limitation we see a good overall agreement between the interlayer spacing steps observed by XRD and predicted from Eqn. (3), is that in these mixed intercalated states one population always strongly dominates the other and is mainly reflected by DSC.

As expected, the amorphous phase fractions are linearly dependent on the interlayer spacing between the platelets, h_{RAF}. From Eqn. (3), w_{RAF} and w_{MAF} are related to h_{RAF} by the relationship $w_{RAF} = \frac{h_{RAF}\rho_{RAF}w_m}{h_m\rho_m}$ and $w_{MAF} = 1 - w_m - \frac{h_{RAF}\rho_{RAF}w_m}{h_m\rho_m}$, respectively. The slopes of the plots of w_{MAF} and w_{RAF} versus w_m for the previously differentiated nanocomposite concentration groups are depicted by the dotted lines in Fig. 4. The slopes of the linear fittings of the different nanocomposite groups (labeled by different colors) clearly depict the changes in interlayer spacings with shifts from group to group. i.e., the group labeled green (0.5–0.65 wt/wt) has an approximately 50% reduction in its slope as compared to the group labeled red (0.05–0.3 wt/wt). This correlates to the 50% reduction in interlayer spacing between the two groups, from 2 to 1 nm as seen in Fig. 3. Another observation is the fact that at very low clay concentrations, < 10% wt/wt, it appears that the model still holds for this regime where the clay morphology is a mixture of exfoliated clay platelets and small tactoids with an average interlayer spacing of 2 nm. This would hint that RAF can also form on the surfaces of the exfoliated clay particles (1 nm on each side), contrary to our assumption that RAF is only located in the interlayer spaces. This cannot be confirmed as many more experimental data points at these very low concentrations, with very precise ΔC_p measurements, would be needed before we can conclude on this issue. It is also quite possible that no RAF would be observed in a completely exfoliated system and that even at our lowest clay concentration, 0.05 wt/wt, the system is still predominately intercalated. Above a w_m of 0.8, all of the MAF is depleted and the w_{RAF} would decrease in a linear two phase model manner as the system is comprised of just RAF and clay.

It is clear by comparing the changes in the RAF and MAF versus

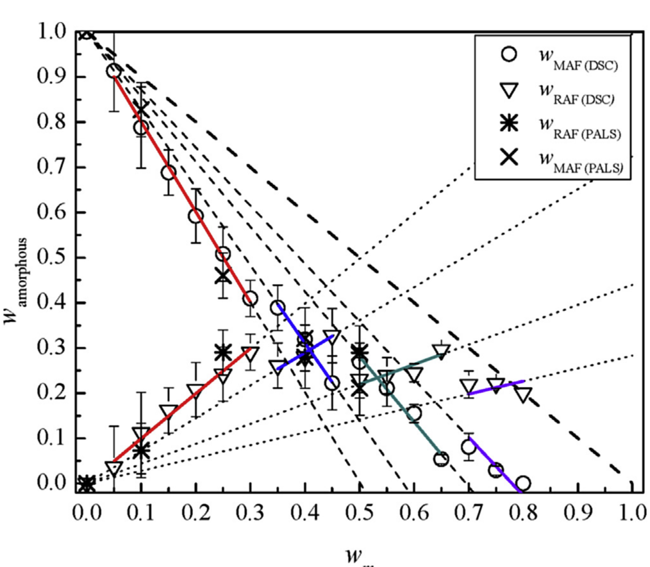

Fig. 4. Weight fractions of MAF (○) and RAF (∇) as determined from ΔC_p and weight fractions of MAF (×) and RAF (⁎) determined from PALS for HBP4 nanocomposites as a function of w_m. The dashed line represents a two-phase model, ie. just MAF and clay. Colored striations represent linear fits of groups of nanocomposites with increasingly smaller interlayer spacings.

clay content trends that the RAF and MAF are dependent upon more than just the fraction of clay within the systems. The changing clay morphologies directly impact RAF formation as well.

Finally, the changes observed by DSC in the bulk glass transition temperature with clay content of the nanocomposites are shown in Fig. 5. The T_g remained near 24 °C at low clay concentrations until it increased between ~10 and 30% wt/wt to a relative plateau region at about 31 °C where it remained until ~50–55% wt/wt clay, where it increased to a final plateau at 36 °C between 60 and 75% wt/wt clay. At and above 80% wt/wt Na^+MMT, T_g detection was not experimentally possible due to the small amplitude of the transition peak at such low polymer concentrations (Fig. 1).

As the T_g is assumed to be solely attributed to the MAF and not the RAF, we believe any increases in T_g with increasing weight fraction of clay loading is a reflection of MAF that has become increasingly affected by proximity to the clay particle surfaces. Thus, we accredit the T_g of these nanocomposites to be a combination of contributions from two MAF populations. The T_g is affected by perturbed MAF regions, situated in the vicinity of the polymer-clay interfaces, and unperturbed MAF regions, situated at large enough distances between the clay tactoids to exhibit the original polymer T_g. The magnitude in the change in T_g will then depend on the relative amounts of perturbed polymer and unperturbed polymer.

We believe, congruent with the data, that the T_g behavior over the different nanoparticle concentration regimes can be explained when analyzed alongside the interlayer spacing and amorphous fraction data in Figs. 3 and 4. At very low concentrations, less than 10% wt/wt clay, the fraction of perturbed regions, existing only at the clay interfaces, is very small and thus the T_g is only slightly effected by the low amount of clay inclusion. From 10 to 30% wt/wt clay, a dramatic increase in T_g is observed, which can be attributed to the sharp overall decrease in MAF (~0.8–~0.4 wt/wt, i.e. red grouping in Fig. 4) taking place in this regime. As the overall MAF is reduced, the amount of perturbed MAF becomes increasingly significant with the development of more interfaces. Within the range 30–50% wt/wt clay, the increase in T_g of the nanocomposite systems becomes much less pronounced. We attribute this relative constant T_g regime, around 31 °C, to the stepwise change in MAF which decreases much less markedly, ~40%–~30% wt/wt, than for the case of constant interlayer spacing. As the interlayer spacings decrease from one differentiated group to another with increased clay content, the clay tactoids incorporate more clay layers per tactoid, but with less RAF constrained in each clay layer, hence the amount of unperturbed MAF can increase. Thus, there is a trade-off in this regime that keeps the apparent T_g relatively constant. Finally, we attribute the last regime of increased T_g, above 55% wt/wt clay, to the small concentration of MAF that remains becoming increasingly perturbed by the clay tactoids as they become closer in proximity.

The success in accurately measuring MAF and RAF content in this nanocomposite system led us to explore the use of positron annihilation lifetime spectroscopy (PALS) which we earlier applied successfully to probe free volume changes in the MAF and RAF in semicrystalline polyethylene terephthalate (PET) [35]. Nanocomposites should prove to be even better suited for this technique as, lacking crystallization, they are much less complex, consisting of only amorphous polymer and thermally stable nanoplatelets.

3.2. Probing the amorphous fractions by PALS

The use of PALS in the analysis of the RAF is novel with only a few attempts in semi-crystalline polymers that have been reported on. Our previous work focused on using PALS to probe the free volume behavior of the RAF and MAF in a semi-crystalline PET

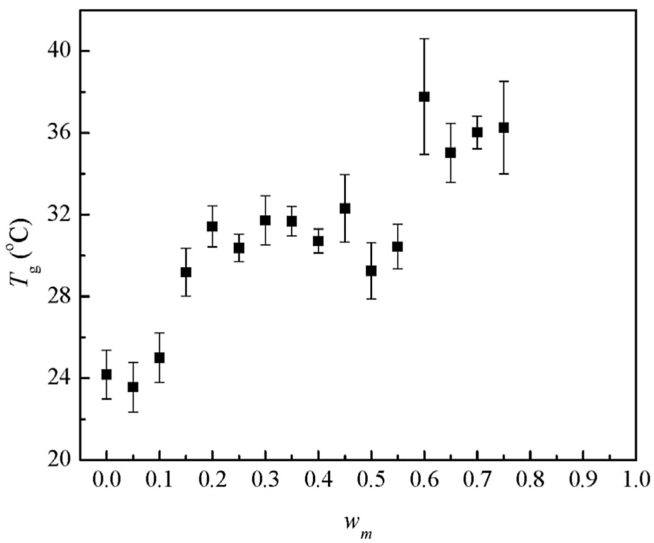

Fig. 5. Glass transition temperature as a function of weight fraction Na^+MMT for HBP4 nanocomposites. Error bars represent standard deviations.

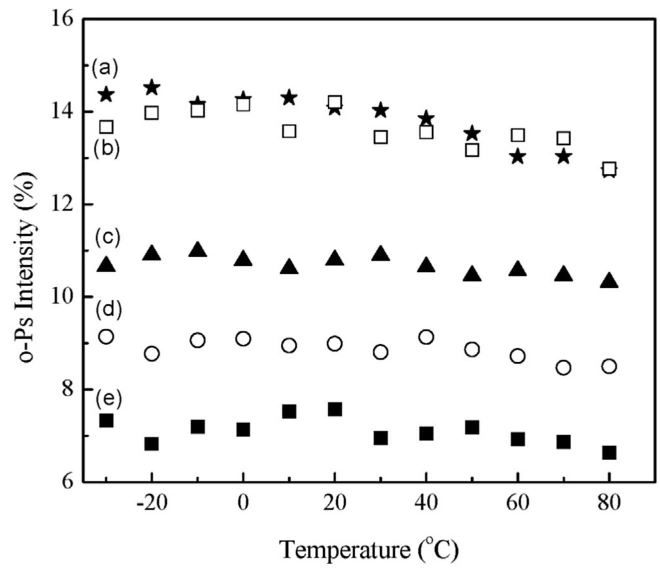

Fig. 6. Orthopositronium intensities, I_3, for HBP4 and Na^+MMT/HBP4 nanocomposites as a function of temperature at the following MMT fractions: (a) 0%, (b) 25%, (c) 40%, (d) 60% and (e) 70% wt/wt.

system [35]. It was confirmed that the RAF exhibited a larger free volume in the glassy state than the MAF at ambient temperature due to the differences in their respective vitrification temperatures. The vitrification temperature for the RAF is the crystallization temperature while the MAF vitrifies at the normal glass transition temperature. This difference results in a larger excess hole free volume accumulated by the RAF upon cooling as compared to the MAF. When both fractions are melted on heating their respective free volumes merge.

To our best knowledge relatively few PALS studies have reported on the free volume in the confined amorphous phase in particulate containing nanocomposites. A few of the early attempts are reviewed in Ref. [76]. Practically all of them were limited by the extent of the mineral phase employed, polymer crystallization, and often by using surfactants, all of which made the analysis of this effect very convoluted. In contrast, the important advantages of our amorphous polymer nanocomposite system include no need of using a surfactant and the fact that these composites can be generated within a very broad range of compositions.

In the present study, we employ positron annihilation lifetime spectroscopy (PALS) in a combination with differential scanning calorimetry (DSC) to analyze the amount and nature of free volume of the RAF and MAF in the Na^+MMT/HBP4 nanocomposite system. The RAF content, quantified from changes in heat capacity with clay content, is compared with estimates using PALS through analysis of the glassy nature of the RAF through changes in the thermal expansivity of free volume holes as a function of clay composition.

To enable this analysis, a few research questions had to be addressed. We needed to determine if o-Ps formed inside the silicate crystals and if the o-Ps had a different probability of forming in the polymer situated in the interlayer spacings (RAF) versus the polymer between the clay stacks (MAF). Finally, we needed to determine if the o-Ps exhibit the same annihilation behavior in the MAF and RAF regimes.

To verify that the contribution of the o-Ps from the clay layers was indeed minimal, a PALS analysis of pure Na^+MMT was performed. The clay was dried for two days under vacuum at 120 °C and then pressed in a mold to form 10 mm by 1 mm discs subjected to PALS analysis. o-Ps lifetimes in the range of 1–10 *ns* were not observed from PALS temperature scans of the clay.

In Fig. 6, we show the temperature dependence of the o-Ps intensities, I_3, for pure HBP4 and Na^+MMT/HBP4 nanocomposites. The o-Ps intensity, I_3, exhibited a weak temperature dependence encompassing the glass and liquid states, typical of amorphous polymers, indicating a corresponding weak temperature dependence in hole density, above and below the T_g [77]. This also suggests that the MAF and RAF regions have consistent hole densities. If the hole densities differed, then one would expect a change in I_3 above the glass transition where only the RAF remains vitrified. Also, increased data scatter causing limited measurement reliability was experienced at high clay concentrations as the amount of polymer to analyze becomes very small, limiting the applicability of some of the data at high concentrations in further analysis.

The o-Ps intensity, I_3, is also plotted as a function of clay filler volume fraction in Fig. 7. The overall o-Ps intensity of the nanocomposite samples decreased linearly with increasing clay content. Similar reductions in I_3 have been observed in other clay

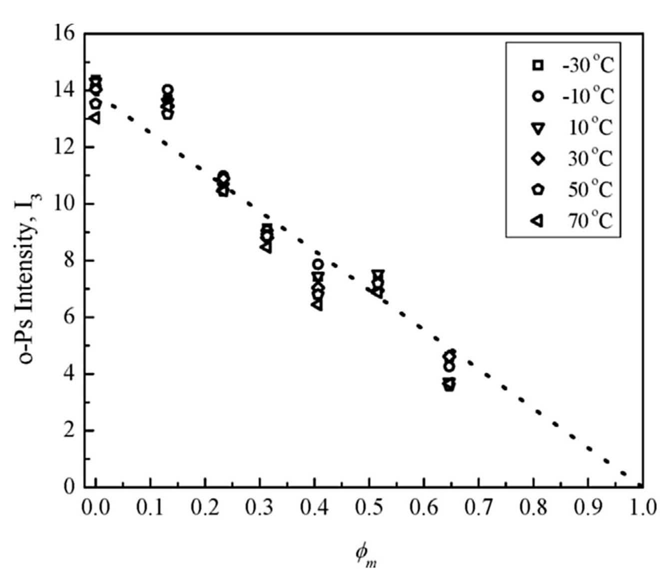

Fig. 7. o-Ps Intensity, I_3, at −30 °C, −10 °C, 10 °C, 30 °C, 50 °C, and 70 °C versus volume fraction Na^+MMT. The dotted line represents a perfect linear correlation between I_3 and the volume fraction of clay.

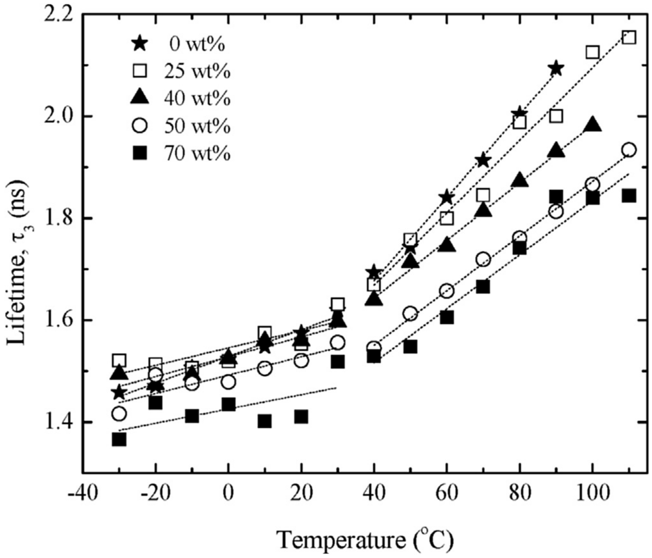

Fig. 8. Orthopositronium lifetimes, τ_3, for HBP4 nanocomposites as a function of temperature at the following MMT fractions: 0%, 25%, 40%, 50% and 70% wt/wt. The dotted lines represent linear fits of the data above and below the T_g.

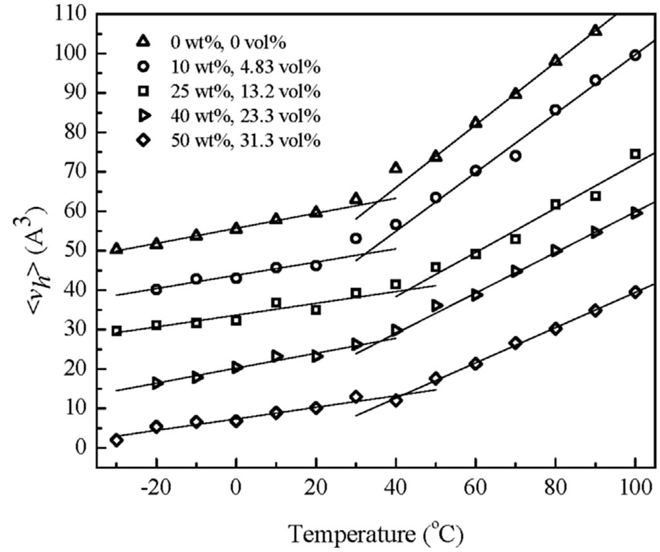

Fig. 9. Hole free volume, v_h, as a function of temperature plots for the nanocomposites. Vertically offset for clarity from 0% vol/vol.

nanocomposite systems [78–80] and in certain semicrystalline systems, such as poly(ether ether ketone) where the o-Ps could not form within the polymer crystallites [81,82]. As mentioned previously, there is negligible positronium formation in the clay layers [83] limiting the regions capable of o-Ps formation to the amorphous polymer phases. Therefore, the linear trend of the o-Ps intensity with clay loading is suggestive of a two phase model dependent only on the polymer fraction and clay content. As there is no noticeable deviation from this two phase model, it can be reasoned that there is a similar probability of o-PS formation in the RAF and MAF regions.

As noted in Eqn. (1), the o-Ps lifetime, τ_3, is directly related to the hole volume in the system. The temperature dependence of τ_3 is shown in Fig. 8. The τ_3 values below T_g for the different clay concentrations remained very similar, as expected, except at very high loadings. While we could speculate on the cause of this decrease in τ_3, e.g. changes in hole shape from increased orientation of the clay, as previously mentioned, data reliability is questionable at high clay concentrations where the relative amount of polymer is small. Therefore, further analysis was confined to clay concentrations at and below 50% wt/wt. Unlike I_3, τ_3 values did increase with temperature, indicative of the expansion of hole sizes on heating. The thermal expansivity of the hole volume was greater above the glass transition temperature, which is reflected in the different slopes of τ_3 with temperature above and below T_g. The slopes of τ_3 with temperature above T_g decreased with increasing clay content, but the slopes below T_g remained relatively constant, irrespective of clay content. This behavior is consistent with the results of Harms et al. in a system of poly(ethylene-alt-propylene) and hydrophobically modified silica nanoparticles [84].

Below T_g, both the amorphous HBP4 confined by the clay layers and the surrounding free HBP4 are in the glassy state. The constant slopes indicate that the thermal expansivity of the RAF phase is equal to that of the pure HBP4 in the glassy state. Above T_g, decreases in the τ_3 versus T slope of the nanocomposites, relative to the slope of the pure HBP4, indicate that a portion of the amorphous phase possesses a lower hole thermal expansivity than the pure HBP4 as the Na^+MMT does not contribute to the o-Ps lifetimes, as established previously. Therefore, above the T_g, the free volume changes detectable by PALS can only be due to contributions from the RAF and MAF phases. Since the RAF exhibited the same thermal expansion properties as the bulk HBP4 in the glassy state, we hypothesized that the decreases in the τ_3 slope of the nanocomposites above T_g, relative to the neat HBP4, are due to the additive contribution of the free volume hole sizes of the RAF and MAF fractions in the nanocomposites, since the RAF is expected to remain vitrified above the bulk T_g.

As the data shows that the MAF and RAF have similar o-Ps concentrations but exhibit different thermal expansivities in hole sizes above the T_g, the possibility to quantify the RAF and MAF phases became clear.

The average hole size, v_h, was calculated by $v_h = (4/3)\pi R^3$, where R is calculated from Eqn. (1), and is plotted in Fig. 9. v_h ranges from 50 to 120 Å^3 over the temperature range studied. The hole thermal expansivity, dv_h/dT, of the vitrified, neat, HBP4 below T_g was taken to be equal to that of the RAF, which remains vitrified by clay confinement above T_g. Since the contributions of RAF and MAF to v_h are considered additive we have the following relationship:

$$v_h = \frac{N^{RAF} v_h^{RAF} + N^{MAF} v_h^{MAF}}{N^{RAF} + N^{MAF}} \quad (4)$$

where v_h is the average hole volume as measured for the composite, v_h^{RAF} is the average hole volume as measured for RAF, and v_h^{MAF} is the average hole volume as measured for MAF. N^{RAF} is the number of free volume holes for the RAF, and N^{MAF} is the number of free volume holes for the MAF. Since this analysis is dependent upon the v_h slopes with temperature, a linear regression of v_h in the glassy state and in the equilibrium liquid state above T_g was required, examples of which are included in Fig. 9. For this linear regression, the data points from 20 to 40 °C are excluded as they are very close to the glass transition. The linear slope of v_h versus T, e_h, for the nanocomposites were thusly defined as:

$$e_h = \frac{dv_h}{dT} \quad (5)$$

and plotted in Fig. 10 where $e_{h\text{-}g}$ and $e_{h\text{-}m}$ refer to the linear slopes below and above the T_g, respectively. Since the slope of the v_h versus T plot for all of the samples below T_g remained constant, the linear slope of the RAF below T_g, dv_h/dT, was defined as e_h^{RAF}. As

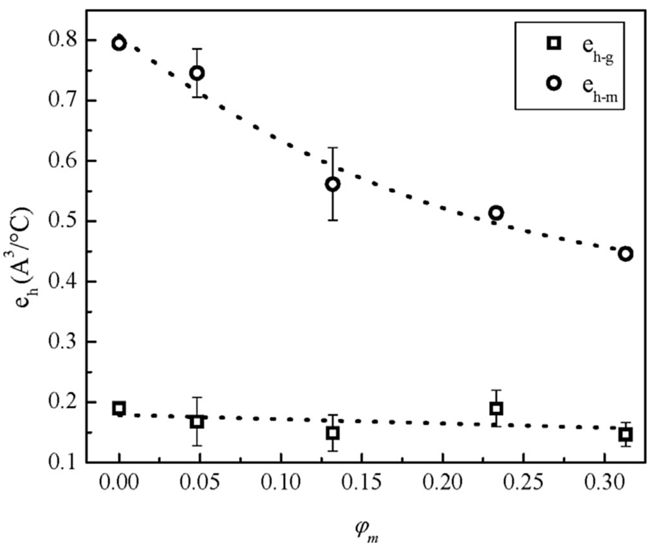

Fig. 10. Thermal expansivity of the nanocomposites systems above (o) and below (□) the T_g. Error bars represent the standard errors of the linear fits from Fig. 9.

there was no HBP4 crystallinity evidenced by DSC or XRD for the pure HBP4 above T_g, the amorphous phase was considered to be composed entirely of MAF and dv_h/dT above T_g was defined as e_h^{MAF}. Based upon the negligible changes of I_3, above and below T_g, we assume that the number density of holes, $n = N_i/V_i$, is the same for RAF and MAF. Since n is constant, Eqn. (4) can be rearranged as follows where $\varphi_{RAF} + \varphi_{MAF} + \varphi_m = 1$.

$$v_h = \frac{\varphi_{RAF} v_h^{RAF} + \varphi_{MAF} v_h^{MAF}}{\varphi_{RAF} + \varphi_{MAF}} \quad (6)$$

Taking the derivative of Eqn. (6) with respect to temperature yields the final equation for the slope of v_h with temperature, with no adjustable parameters.

$$e_{h-m} = \frac{\varphi_{RAF} e_h^{RAF} + \varphi_{MAF} e_h^{MAF}}{\varphi_{RAF} + \varphi_{MAF}} \quad (7)$$

Employing Eqn. (7) allowed for φ_{RAF} and φ_{MAF} to be extracted from the slope, $e_{h\text{-}m}$, of the v_h plots with temperature. The slope below T_g, e_h^{RAF}, was 0.19 Å^3/°C and the slope above T_g, e_h^{MAF}, was 0.80 Å^3/°C for the pure HBP4. The correlation coefficients were at or above 0.99 for the linear regression analysis, and the results from the v_h slope analysis are summarized in Table 2. The resulting φ_{RAF} and φ_{MAF} determined from this analysis are shown in Table 2 and plotted in Fig. 4 relative to the loading fraction of Na$^+$MMT. The volume fractions of the amorphous phases as determined by the previous DSC analysis are included for comparative purposes in Table 2.

As seen in Table 2, the volume fractions of amorphous HBP4 determined from the o-Ps lifetime analysis are similar to those determined from analyzing the ΔC_p at T_g. This provides additional evidence that the RAF phase remains vitrified well above T_g due to the constraints imposed by the surfaces of the montmorillonite clay layers. Therefore, it was clearly demonstrated by both the bulk thermal and nanoscopic free volume techniques that the adsorption, flattening, and confinement of the HBP lead to the vitrification of a portion of the HBP, which remains vitrified well above the bulk T_g.

4. Conclusions

A broad concentration range of nanocomposites, based on the fourth generation of a Boltorn™ dendritic polyol (HBP4) combined with unmodified sodium montmorillonite clay (Na$^+$MMT), was prepared using water as a solvent (0–100% wt/wt Na$^+$MMT). The HBP4 exhibits a DSC glass transition temperature ~24 °C, followed by exothermic and endothermic events, attributed to the formation and melting of an ordered mesophase, whose formation is suppressed on addition of clay to form a nanocomposite.

With the addition of clay, the bulk T_g exhibited a modest increase, while the ΔC_p at T_g showed a substantial decrease. The ΔC_p behavior for the nanocomposites deviated significantly from the linear trend expected for a two-phase composite in an unusual step-like fashion indicative of suppression of the segmental mobility of the amorphous HBP polymer. At and above 80% wt/wt of clay, the glass transition in the nanocomposites was fully suppressed. The step-like deviation from the two-phase prediction was demonstrated to correlate to step-like changes in intercalation interlayer spacing groupings observed in a previous study [28]. The weight fraction of the MAF (w_{MAF}), which contributed to the step in the heat capacity at T_g was calculated based on the corresponding ΔC_p. A simple series mathematical model in which multiple confined polymer layers alternate between mineral layers enabled calculation of interlayer spacings from the experimental ΔC_p data which were in excellent agreement with those determined by XRD.

From knowledge of w_{MAF} for each clay content we were able to calculate the amount of RAF (since $w_m + w_{RAF} + w_{MAF} = 1$). As much as ~32% wt/wt of the system was made up of RAF at its maximum. Incremental steps in interlayer spacings observed at 0.3–0.35, 0.45–0.5, and 0.65–0.7 wt/wt clay correlated to abrupt increases in w_{MAF} (decrease in w_{RAF}) at each step, followed by a linear decrease in w_{MAF} (increase in w_{RAF}) with increasing clay content until the next step is reached. Clearly, the changes in the RAF and MAF content depend not only on the fraction of clay within the system but also on the changes in clay morphology.

As the T_g is attributed solely to the MAF and not the immobilized RAF, we believe the observed increases in T_g with increasing weight fraction of clay loading are a reflection of a MAF fraction whose mobility has become perturbed by the proximity to the clay particles. Thus, we attribute the T_g of these nanocomposites to be a result of the combination of two distinct MAF populations, perturbed and unperturbed MAF situated at large enough distances between the clay tactoids to exhibit the bulk polymer T_g. The magnitude of the change in T_g then depends on the relative

Table 2
Amorphous volume fractions determined from the free volume temperature coefficients of HBP4 nanocomposites.

w_m	φ_m	$e_{h\text{-}g}$ (Å^3/°C)	$e_{h\text{-}m}$ (Å^3/°C)	φ_{MAF} (PALS)	φ_{MAF} (ΔC_p)	φ_{RAF} (PALS)	φ_{RAF} (ΔC_p)
0	0	0.19 ± 0.01	0.80 ± 0.01	1.00	1.00	0.00	0.00
0.10	0.048	0.17 ± 0.04	0.75 ± 0.04	0.88 ± 0.07	0.83 ± 0.10	0.08 ± 0.07	0.12 ± 0.10
0.25	0.132	0.15 ± 0.03	0.56 ± 0.06	0.53 ± 0.06	0.59 ± 0.07	0.34 ± 0.06	0.28 ± 0.07
0.40	0.233	0.19 ± 0.03	0.51 ± 0.01	0.41 ± 0.02	0.41 ± 0.09	0.36 ± 0.02	0.36 ± 0.09
0.50	0.313	0.15 ± 0.02	0.45 ± 0.01	0.29 ± 0.02	0.37 ± 0.11	0.37 ± 0.02	0.32 ± 0.11

amounts of each population.

Positron annihilation spectroscopy (PALS) was used to gain information on the temperature dependence of free volume hole density and average hole sizes from I_3 and τ_3, respectively encompassing the glassy and liquid states. The weak temperature dependence of I_3 indicated similar o-Ps formation probabilities in RAF and MAF. This enabled a novel nanocopic approach to estimate w_{RAF} and w_{MAF} via PALS from the thermal expansivities of hole sizes in the liquid and glassy states. The volume fractions of RAF and MAF of the HBP4 nanocomposites determined from o-Ps lifetime analysis proved to be consistent with those determined from analysis of ΔC_p at T_g. This serves to verify the glassy nature of the RAF constrained by the montmorillonite layers at elevated temperatures.

Acknowledgements

The authors are grateful to the National Science Foundation for support of this work through the Center for Layered Polymeric Systems (DMR-0423914) and MRSEC (DMR-0213883).

Appendix A. Supplementary data

Supplementary data related to this article can be found at http://dx.doi.org/10.1016/j.polymer.2017.01.065.

References

[1] M. Alexandre, P. Dubois, Polymer-layered silicate nanocomposites: preparation, properties, and uses of a new class of materials, Mat. Sci. Eng. 28 (2000) 1.
[2] S.S. Ray, M. Okamoto, Polymer/layered silicate nanocomposites: a review from preparation to processing, Prog. Polym. Sci. 28 (2003) 1539.
[3] S.C. Tjong, Structural and mechanical properties of polymer nanocomposites, Mat. Sci. Eng. 53 (2006) 73.
[4] K.E. Strawhecker, E. Manias, Structure and properties of poly(vinyl alcohol)/Na montmorillonite nanocomposites, Chem. Mater 12 (2000) 2943.
[5] M. Jikei, M. Kamimoto, Hyperbranched polymers: a promising new class of materials, Prog. Polym. Sci. 26 (2001) 1233.
[6] P.W. Zhu, S. Zheng, G. Simon, Dielectric relaxations in a hyperbranched polyester with terminal hydroxyl groups: effects of generation number, Macromol. Chem. Phys. 202 (2001) 3008.
[7] A. Luciani, C.J.G. Plummer, T. Nguyen, L. Garamszegi, J.E. Manson, Rheological and physical properties of aliphatic hyperbranched polyesters, J. Polym. Sci. Part B Polym. Phys. 42 (2004) 1218.
[8] E. Žagar, M. Žigon, Characterization of a commercial hyperbranched aliphatic polyester based on 2,2-Bis(methylol)propionic acid, Macromolecules 35 (2002) 9913.
[9] E. Žagar, M. Huskić, M. Žigon, Macrom. Structure-to-Properties relationship of aliphatic hyperbranched polyesters, Chem. Phys. 208 (2007) 1379.
[10] E. Žagar, M. Huskić, J. Grdadolnik, M. Žigon, A. Zupanćić-Valant, Effect of annealing on the rheological and thermal properties of aliphatic hyperbranched polyester based on 2,2-Bis(methylol)propionic acid, Macromolecules 38 (2005) 3933.
[11] E. Žagar, M. Žigon, S. Podzimek, Characterization of commercial aliphatic hyperbranched polyesters, Polymer 47 (2006) 166.
[12] I. Tanis, K. Karatasos, Local dynamics and hydrogen bonding in hyperbranched aliphatic polyesters, Macromolecules 42 (2009) 9581.
[13] E. Malmström, M. Johansson, A. Hult, Hyperbranched aliphatic polyesters, Macromolecules 28 (1995) 1698.
[14] A. Burgath, A. Sunder, H. Frey, Role of cyclization in the synthesis of hyperbranched aliphatic polyesters, Macromol. Chem. Phys. 201 (2000) 782.
[15] E. Malmström, A. Hult, Kinetics of formation of hyperbranched polyesters based on 2,2-bis(methylol)propionic acid, Macromolecules 29 (1996) 1222.
[16] H. Magnusson, E. Malmström, A. Hult, Structure buildup in hyperbranched polymers from 2,2-Bis(hydroxymethyl)propionic acid, Macromolecules 33 (2000) 3099.
[17] T. Zeiner, P. Shrader, S. Enders, D.J. Browarzik, Phase- and interfacial behavior of hyperbranched polymer solutions, Fluid Phase Equilib. 302 (2011) 321.
[18] V.V. Tsukruk, Dendritic macromolecules at interfaces, Adv. Mater 10 (3) (1998) 253.
[19] S. Peleshanko, V.V. Tsukruk, The architectures and surface behavior of highly branched molecules, Prog. Polym. Sci. 33 (2008) 523.
[20] V.V. Tsukruk, F. Rinderspacher, V.N. Bliznyuk, Self-assembled multilayer films from dendrimers, Langmuir 13 (1997) 2171.
[21] M.S. Bakshi, R. Sood, G. Kaur, K. Sakai, T. Yoshimura, K. Esumi, Characterization of aliphatic and aromatic polyester hyperbranched dendrimers by AFM imaging, Colloid Polym. Sci. 284 (2005) 74.
[22] S.S. Sheiko, A.M. Musafarov, R.G. Winkler, E.V. Getmanova, G. Eckert, P. Reineker, Contact angle microscopy on a carbosilane dendrimer with hydroxyl end groups: method for mesoscopic characterization of the surface structure, Langmuir 13 (1997) 4172.
[23] M.L. Mansfield, Surface adsorption of model dendrimers, Polymer 37 (17) (1996) 3835.
[24] C.J.G. Plummer, L. Gramszegi, Y. Leterrier, M. Rodlert, J.E. Månson, Hyperbranched polymer layered silicate nanocomposites, Chem. Mater 14 (2002) 486.
[25] M. Rodlert, C.J.G. Plummer, H.J.M. Grünbauer, J.E. Månson, Hyperbranched polymer/clay nanocomposites, Adv. Eng. Mater 6 (9) (2004) 715.
[26] M. Rodlert, C.J.G. Plummer, L. Gramszegi, Y. Leterrier, H.J.M. Grunbauer, J.E. Månson, Hyperbranched polymer/montmorillonite clay nanocomposites, Polymer 45 (2004) 949.
[27] M. Rodlert, C.J.G. Plummer, Y. Leterrier, J.E. Månson, Rheological behavior of hyperbranched polymer/montmorillonite clay nanocomposites, J. Rheol. 48 (5) (2004) 1049.
[28] J.J. Decker, S.N. Chvalun, S. Nazarenko, Intercalation behavior of hydroxylated dendritic polyesters in polymer clay nanocomposites prepared from aqueous solution, Polymer 52 (2011) 3943.
[29] K. Androulaki, K. Chrissopoulou, D. Prevosto, M. Labardi, S.H. Anastasiadis, Dynamics of hyperbranched polymers under confinement: a dielectric relaxation study, ACS Appl. Mat. Interfaces 7 (2015) 12387.
[30] S. Fotiadou, C. Karageorgaki, K. Chrissopoulou, K. Karatasos, I. Tanis, D. Tragoudaras, B. Frick, S.H. Anastasiadis, Structure and dynamics of hyperbranched polymer/layered silicate nanocomposites, Macromolecules 46 (2013) 2842.
[31] A.U. Liyanage, E.U. Ikhuoria, A.A. Adenuga, V.T. Remcho, M.M. Lerner, Synthesis and characterization of low-generation polyamidoamine (PAMAM) dendrimer-sodium montmorillonite (Na-MMT) clay nanocomposites, Inorg. Chem. 52 (2013) 4603.
[32] B. Wunderlich, Reversible crystallization and the rigid—amorphous phase in semicrystalline macromolecules, Prog. Polym. Sci. 28 (2003) 383.
[33] B. Wunderlich, Calorimetry of nanophases of macromolecules, Int. J. Thermophys. 28 (2007) 958.
[34] J. Lin, S. Shenogin, S. Nazarenko, Oxygen solubility and specific volume of rigid amorphous fraction in semicrystalline poly(ethylene terephthalate), Polymer 43 (2002) 4733.
[35] B.G. Olson, J. Lin, S. Nazarenko, A.M. Jamieson, Positron annihilation lifetime spectroscopy of poly(ethylene terephthalate): contributions from rigid and mobile amorphous fractions, Macromolecules 36 (2003) 7618.
[36] M.C. Righetti, E. Tombari, M.L. Di Lorenzo, The role of the crystallization temperature on the nanophase structure evolution of poly[(r)-3-hydroxybutyrate], J. Phys. Chem. B 117 (2013) 12303.
[37] M.L. Di Lorenzo, R. Androsch, I. Stolte, Tailoring the rigid amorphous fraction of isotactic polybutene-1 by ethylene chain defects, Polymer 55 (2014) 6132.
[38] F. Hamonic, V. Miri, A. Saiter, E. Dargent, Rigid amorphous fraction versus oriented amorphous fraction in uniaxially drawn polyesters, Eur. Polym. J. 58 (2014) 233.
[39] B.S. Beckingham, V. Ho, R.A. Segalman, formation of a rigid amorphous fraction in poly(3-(2'-ethyl) hexylthiophene), ACS Macro Lett. 3 (2014) 684.
[40] M.C. Righetti, M. Laus, M.L. Di Lorenzo, Temperature dependence of the rigid amorphous fraction in poly(ethylene terephthalate), Eur. Polym. J. 58 (2014) 60.
[41] M.C. Righetti, M. Laus, M.L. Di Lorenzo, Rigid amorphous fraction and melting behavior of poly(ethylene terephthalate), Colloid Polym. Sci. 292 (2014) 1365.
[42] S. Tognana, W. Salgueiro, Influence of the rigid amorphous fraction and segregation during crystallization in PHB/DGEBA blends, Polym. J. (2015) 1.
[43] C.A. Massa, S. Pizzanelli, V. Bercu, L. Pardi, D. Leporini, Constrained and heterogeneous dynamics in the mobile and the rigid ammorphous fractions of poly(dimethylsiloxane): a multifrequency high-field electron paramagnetic resonance study, Macromolecules 47 (2014) 6748.
[44] R. Remy, S. Wei, L.M. Campos, M.E. Mackay, Three-phase morphology of semicrystalline polymer semiconductors: a quantitative analysis, ACS Macro Lett. 4 (2015) 1051.
[45] A. Sargsyan, A. Tonoyan, S. Davtyan, C. Schick, The amount of immobilized polymer in PMMA SiO_2 nanocomposites determined from calorimetric data, Eur. Polym. J. 43 (2007) 3113.
[46] E.C. Corcione, A. Maffezzoli, Glass transition in thermosetting clay-nanocomposite polyurethanes, Thermochim. Acta 485 (2009) 43.
[47] A. Wurm, M. Ismail, B. Kretzschmar, D. Pospiech, C. Schick, Retarded crystallization in polyamide/layered silicates nanocomposites caused by an immobilized interphase, Macromolecules 43 (2010) 1480.
[48] S. Fotiadou, K. Chrissopoulou, B. Frick, S.H. Anastasiadis, Structure and dynamics of polymer chains in hydrophilic nanocomposites, J. Polym. Sci. Part B Polym. Phys. 48 (2010) 1658.
[49] M.G. Sari, M. Shahbazi, A.S. Pakdel, Developing a novel hyperbranched polymer-modified PP/clay nanocomposite: characteristics investigation, Polymer-Plastics Technol. Eng. 53 (2014) 1561.
[50] A. Sargsyan, A. Tonoyan, S. Davtyan, C. Schick, The amount of immobilized polymer in PMMA SiO_2 nanocomposites determined from calorimetric data, Eur. Polym. J. 43 (2007) 3113.
[51] A. Sargsyan, A. Tonoyan, S. Davtyan, C. Schick, Rigid amorphous fraction in polymer nano-composites, NATAS Notes 39 (2007) 6.

[52] P. Pissis, P. Klonos, A. Kyritsis, Interfacial Effects in Polymer Nanocomposites Studied by Dielectric and Thermal Techniques, IEEE, 2011, p. 67.
[53] S.P. Davtyan, A.O. Tonoyan, A.Z. Varderesyan, S.C. Muller, Frontal compolymerization in the presence of nano-particles, Eur. Polym. J. 57 (2014) 182.
[54] S. Kim, N.A. Nguyen, J.J. Wie, H.S. Park, Manipulating the glass transition behavior of sulfonated polystyrene by functionalized nanoparticle inclusion, Nanoscale 7 (2015) 8864.
[55] K. Chrissopoulou, S. Fotiadou, B. Frick, S.H. Anastasiadis, Structure and dynamics in hydrophilic polymer/layered silicate nanocomposites, Macromol. Symp. 331–332 (2013) 50.
[56] F. Signori, M. Pelagaggi, S. Bronco, M.C. Righetti, Amorphous/crystal and polymer/filler interphases in biocomposites from poly(butylene succinate), Thermochim. Acta 543 (2012) 74.
[57] S. Karami, P.G. Lafleur, Role of chain dynamics and topological confinements in cold crystallization of PLA-clay nanocomposites, Polym. Eng. Sci. 55 (2015) 1310.
[58] P. Klonos, S. Kripotou, A. Kyritsis, G.Z. Papageorgiou, D. Bikiaris, D. Gournis, P. Pissis, Glass transistion and segmental dyanmics in poly(L-lactic acid)/graphene oxide nanocomposites, Thermochim. Acta 617 (2015) 44.
[59] S. Charlon, S. Marais, E. Dargent, J. Soulestin, M. Sclavons, N. Follain, Structure-barrier property relationship of biodegradable poly(butylene succinate) and poly[(butylene succinate)-co-(butylene adipate)] nanocomposites: influence of the rigid amorphous fraction, Phys. Chem. Chem. Phys. 17 (2015) 29918.
[60] S.K. Rath, K. Sudarshan, R.S. Bhavsar, U.K. Kharul, P.K. Pujari, M. Patri, D.V. Khakhar, Characterizing the nanoclay induced constrained amorphous region in model segmented polyurethane-urea/clay nanocomposites and its implications on gas barrier properties, Phys. Chem. Chem. Phys. 18 (2016) 1487.
[61] P.J. Purohit, D. Wang, A. Wurm, C. Schick, A. Schonhals, Eur. Polym. J. 55 (2014) 48.
[62] S. Fotiadou, C. Karageorgaki, K. Chrissopoulou, K. Karatasos, I. Tanis, D. Tragoudaras, B. Frick, S.H. Anastasiadis, Structure and dynamics of hyperbranched polymer/layered silicate nanocomposites, Macromolecules 46 (2013) 2842.
[63] R.A. Pethrick, Positron annihilation—a probe for nanoscale voids and free volume? Prog. Polym. Sci. 22 (1997) 1.
[64] Y.C. Jean, P.E. Mallon, D.M. Schrader (Eds.), Principles and Applications of Positron and Positronium Chemistry, World Scientific, River Edge, NJ, 2003.
[65] H. Higuchi, Z. Yu, A.M. Jamieson, R. Simha, J.D. McGervey, Thermal history and temperature dependence of viscoelastic properties of polymer glasses: relation to free volume quantities, J. Polym. Sci. Polym. Phys. 33 (17) (1995) 2295.
[66] R. Simha, T. Somcynsky, On the statistical thermodynamics of spherical and chain molecule fluids, Macromolecules 2 (1969) 342.
[67] M. Eldrup, D. Lightbody, N.J. Sherwood, The temperature dependence of positron lifetimes in solid pivalic acid, Chem. Phys. 63 (1981) 51.
[68] S.J. Tao, Positronium annihilation in molecular substances, J. Chem. Phys. 56 (1972) 5499.
[69] G. Lagaly, S. Ziesmer, Colloid chemistry of clay minerals: the coagulation of montmorillonite dispersions, Adv. Colloid Interface Sci. 100 (2002) 105.
[70] G. Carmezini, M.E. Mackay, B.B. Sauer, W. Kampert, Manipulation of hyperbranched polymers' conformation, Chem. Mater 14 (2002) 819.
[71] S.Z.D. Cheng, M.-Y. Cao, B. Wunderlich, Glass transition and melting behavior of poly(oxy-1,4-phenyleneoxy-1,4-phenylenecarbonyl-1,4-phenylene) (PEEK), Macromolecules 19 (1986) 1868.
[72] M.J. Richardson, in: V.B.F. Mathot (Ed.), Calorimetry and Thermal Analysis of Polymers, Hanser, Munich, 1993, p. 170.
[73] P. Kirkegard, M. Eldrup, O.E. Morgesen, N.J. Pedersen, Program system for analysing positron lifetime spectra and angular correlation curves, Comput. Phys. Commun. 23 (1981) 307.
[74] J. Grebowicz, S.F. Lau, B.J. Wunderlich, The thermal properties of polypropylene, J. Polym. Sci. Polym. Symp. 71 (1984) 19.
[75] H. Suzuki, J. Grebowicz, B.J. Wunderlich, Heat capacity of semicrystalline, linear poly(oxymethylene) and poly(oxyethylene), Macromol. Chem. 186 (1985) 1109.
[76] A.M. Jamieson, B.G. Olson, S. Nazarenko, Positron annihilation lifetime studies of free volume in heterogeneous polymer systems, in: L. Utrackie, A. Jamieson (Eds.), Polymer Physics: from Suspensions to Nanocomposites and beyond, John Wiley & Sons, Inc., Hoboken, NJ, 2010, p. 473.
[77] Z. Yu, U. Yahsi, J.D. McGervey, A.M. Jamieson, R. Simha, Molecular weight-dependance of free volume in polystyrene studied by positron annihilation measurements, J. Polym. Sci. Pol. Phys. 32 (1994) 2637.
[78] G. Choudalakis, A.D. Gotsis, Free volume and mass transport in polymer nanocomposites, Curr. Opin. Colloid Interface Sci. 17 (2012) 132.
[79] Y.-Q. Wang, Y.-P. Wu, H.-F. Zhange, L.-Q. Zhang, B. Wang, Z.-F. Wang, Free volume of montmorillonite/styrene-butadiene rubber nanocomposites estimated by positron annihilation lifetime spectroscopy, Macromol. Rapid Commun. 25 (2004) 1973.
[80] Z.F. Wang, B. Wang, N. Qi, H.F. Zhang, L.Q. Zhang, Influence of fillers on free volume and gas barrier properties in styrene-butadiene rubber studied by positrons, Polymer 46 (2005) 719.
[81] H. Nakanishi, Y.C. Jean, Dynamics of excess free volume in semicrystalline peek studied by positron annihilation, Macromolecules 24 (1991) 6618.
[82] H. Nakanishi, Y.C. Jean, positronium formation at free-volume sites in the amorphous regions of semicrystalline peek, J. Polym. Sci. B 1989 (1419) 27.
[83] M. Sano, H. Murakami, K. Ichimura, Positronium in a layered-structure material: montmorillonite, J. Radioanal. Nucl. Chem. 239 (2) (1999) 325.
[84] S. Harms, K. Rätzke, F. Faupel, G.J. Schneider, L. Willner, D. Richter, Free volume of interphases in model nanocomposites studied by positron annihilation lifetime spectroscopy, Macromolecules 43 (2010) 10505.